Synthesis and evaluation of [^{11}C]MCC950 for imaging NLRP3-mediated inflammation in atherosclerosis

Uzair S. Ismailani,[1,2] Ariel Buchler,[2,3] Nicole MacMullin,[2] Faduma Abdirahman,[2,3] Myriam Adi,[2,3] Benjamin H. Rotstein[1,2,3]*

[1] Department of Biochemistry, Microbiology and Immunology, University of Ottawa, Ottawa, Ontario, Canada

[2] University of Ottawa Heart Institute, Ottawa, Ontario, Canada

[3] Department of Chemistry and Biomolecular Sciences, University of Ottawa, Ottawa, Ontario, Canada.

Correspondence: Benjamin H. Rotstein, PhD
University of Ottawa Heart Institute
40 Ruskin Street, H-5219
Ottawa, Ontario, Canada
K1Y 4W7
Phone: 613-696-7324
Email: benjamin.rotstein@uottawa.ca

Abstract

Overexpression of the NLRP3 inflammasome has been attributed to the progressive worsening of a multitude of cardiovascular inflammatory diseases such as myocardial infarction, pulmonary arterial hypertension, and atherosclerosis. The recently discovered potent and selective NLRP3 inhibitor MCC950 has shown promise in hindering disease progression but NLRP3-selective cardiovascular positron emission tomography imaging has not yet been demonstrated. We synthesized [^{11}C]MCC950 with no-carrier-added [^{11}C]CO_2 fixation chemistry using an iminophosphorane precursor (RCY 45 ± 4 %, >99% RCP, 27 ± 2 GBq/μmol, 23 ± 3 min, n = 6) and determined its distribution both *in vivo* and *ex vivo* in C57BL/6 and atherogenic *ApoE*$^{-/-}$ mice. Small animal PET imaging was performed in both strains following intravenous administration via the lateral tail vein and revealed considerable uptake in the liver that stabilized by 20 minutes (7–8.5 SUV), coincident with secondary renal excretion. Plasma metabolite analysis uncovered excellent *in vivo* stability of [^{11}C]MCC950 (94% intact. *Ex vivo* autoradiography performed on excised aortas revealed heterogenous uptake in atherosclerotic plaques of *ApoE*$^{-/-}$ mice in comparison to C57BL/6 controls (48 ± 17 %ID/m^2 vs 18 ± 8 %ID/m^2, p = 0.002, n = 4-5). Treatment of *ApoE*$^{-/-}$ mice with nonradioactive MCC950 (5 mg/kg, iv) 10 minutes prior to radiotracer administration increased uptake in intestines (5.3 ± 1.8 %ID/g vs 11.0 ± 3.7 %ID/g, p = 0.04, n = 4-6) and in aortic lesions (48 ± 17 %ID/m^2 vs 104 ± 15 %ID/m^2, p = 0.0002, n = 5) by 108% and 117%, respectively, without significantly increasing plasma free fraction (f_p, 1.3 ± 0.4% vs 1.7 ± 0.8%, n = 2). These results suggest that [^{11}C]MCC950 uptake demonstrates specific binding and may prove useful for *in vivo* NLRP3 imaging in atherosclerosis.

Keywords: NOD-like receptor pyrin domain-containing protein 3 (NLRP3); atherosclerosis; molecular imaging; autoradiography; positron emission tomography; MCC950; carbon-11; CO_2-fixation

Introduction

Atherosclerosis is a chronic inflammatory disease that is characterized by the thickening and hardening of arterial walls due to the deposition of lipids, infiltration of leukocytes, and proliferation of vascular smooth muscle cells.[1,2] The resulting lesions are generally asymptomatic in early stages, but continual growth and inflammation result in the formation of unstable plaques that are prone to ruptures and consequent angina, myocardial infarction, and sudden cardiac death.[1,3] Increasing evidence suggests that the progression of atherosclerosis is driven by the aberrant activation of the innate immune system and upregulation of inflammasomes.[4–6]

Inflammasomes are cytoplasmic multi-protein complexes found in macrophages and microglia. They comprise oligomers of NOD-like receptor (NLR) protein, apoptosis-associated speck-like protein containing a caspase recruitment domain (ASC), and caspase-1, a cysteine protease that processes proinflammatory cytokines. Specifically, cytokines such as IL-1β and IL-18 are matured by caspase-1 and are markedly upregulated in atherosclerosis due to increased expression of the NLRP3 inflammasome.[4,6] Extracellular danger-associated molecular patterns (DAMPs), such as free fatty acids, activate toll-like receptor 4 (TLR4) on the surface of macrophages and induce NF-κB-dependent transcription of pro-IL-1β and monomeric NLRP3.[4,7] Additionally, receptor-mediated phagocytosis of cholesterol crystals or oxidized low-density lipoprotein (LDL) destabilizes phagolysosomes, releasing cathepsin B and amplifying NLRP3 inflammasome assembly.[4,6,7] Chronic stimulation of this pathway promotes sterile inflammation and the development of atheromas. However, NLRP3 inflammasome inhibitors have shown considerable promise in attenuating disease progression.[8–14]

The diaryl sulfonylurea MCC950 is a first-in-class potent and selective NLRP3 inhibitor (IC_{50} = 8 nM) shown to have excellent anti-inflammatory activity *in vivo*.[15] MCC950 has demonstrated the considerable potential of NLRP3 inhibition against a multitude of inflammatory disease models including

neurodegenerative disorders, autoimmune conditions, and cardiovascular diseases, among others.[16] While current literature suggests that MCC950 accesses the central nervous system (CNS) at therapeutic doses,[16] its recent *in vivo* evaluation as a positron emission tomography (PET) radiotracer revealed poor blood brain barrier (BBB) penetration at microdoses, limiting its use for brain imaging.[17]

Carbon-11 is revered for isotopic labeling of biologically relevant molecules but its use is limited by the synthetic methods available for incorporating it into diverse functional groups.[18,19] Radiolabeled sulfonylureas can be synthesized by rhodium-mediated [^{11}C]CO carbonylation of a sulfonyl azide and an amine (Scheme 1).[20–22] However, the availability of [^{11}C]CO is constrained to a small number of PET research facilities as it requires specialized infrastructure and equipment to produce. These drawbacks are indicative of the growing need for inexpensive and efficient strategies to label sulfonylureas directly from [^{11}C]CO_2. Cyclotron-produced [^{11}C]CO_2 can be converted into more reactive intermediates following stepwise trapping and dehydration using phosphorous oxychloride ($POCl_3$) or Mitsunobu reagents to yield ^{11}C-isocyanates.[19,23,24] Indeed, Mitsunobu conditions were used to prepare [^{11}C]MCC950 from carrier-added [^{11}C]CO_2 in low radiochemical yield (RCY) and low molar activity.[17] The challenge lies in the condensation of the sterically hindered aromatic 4-amino-1,2,3,5,6,7-hexahydro-s-indacene (**1**) with [^{11}C]CO_2 and addition of the weakly nucleophilic furyl sulfonamide (**2**) to the ^{11}C-isocyanate intermediate.

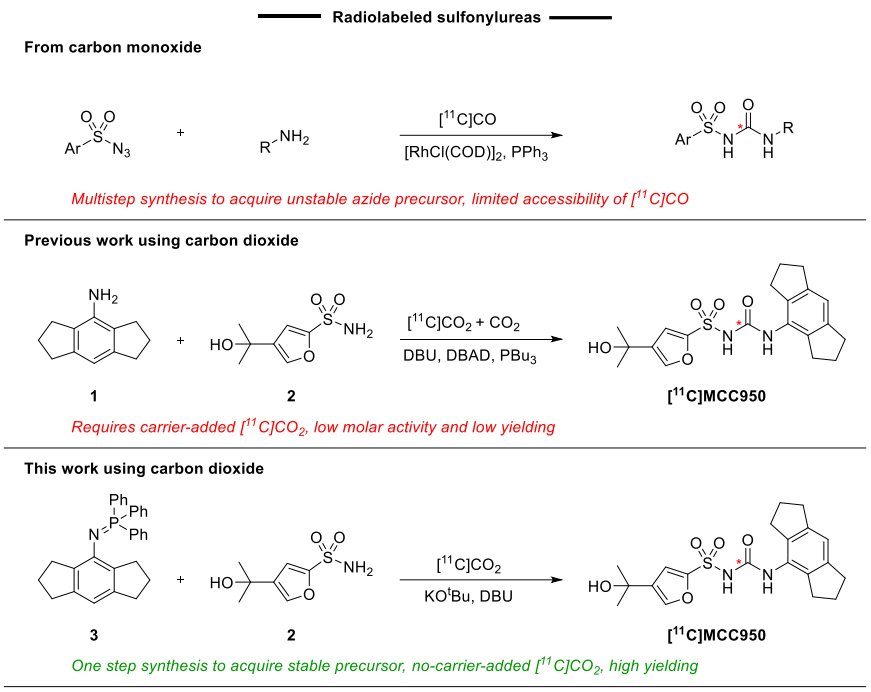

Scheme 1. Radiosynthetic methods to label ^{11}C-sulfonylureas

Our goal was to develop a high-yielding reliable synthesis of [^{11}C]MCC950 using our previously developed iminophosphorane [^{11}C]CO_2-fixation methods,[25] and to evaluate this probe for detecting atheromas in *ApoE*$^{-/-}$ mice. Our *in vivo* and *ex vivo* evaluation includes small animal PET imaging and biodistribution to determine tracer kinetics, metabolite analysis to assess tracer stability, and autoradiography under baseline and homologous blockade conditions to detect probe specificity towards NLRP3-mediated inflammation in atheromas.

Materials and methods

Animal models

Male C57BL/6J (strain #000664) and *ApoE*$^{-/-}$ (strain #002052) mice were purchased from Jackson Laboratory and acclimated upon arrival for 1 week. Animals were housed in groups of four and monitored periodically until 12–14 weeks of age. C57BL/6 mice were kept on normal chow diet whereas *ApoE*$^{-/-}$ mice

were fed western atherogenic diet (TD.88137, Envigo) from 6 weeks of age. Both animal strains were provided with free access to food and water and housed in environmentally enriched cages. Animal handling, housing, and experimental procedures were conducted in strict accordance with the guidelines of Canadian Council on Animal Care and received approval of the University of Ottawa Animal Care Committee.

Synthesis of N-(triphenylphosphoranylidene)-1,2,3,5,6,7-hexahydro-s-indacen-4-amine (3)

A flame dried flask was equipped with a magnetic stir bar and charged with triphenylphosphine dibromide (0.60 mmol) under inert atmosphere and dissolved in DCM (5.0 mL). The flask was placed in an ice bath, and a solution containing 4-amino-1,2,3,5,6,7-hexahydro-s-indacene (**1**, 0.57 mmol) and triethylamine (1.73 mmol) in DCM (5 mL) was added to the reactor in a dropwise manner over 10 minutes. The flask was placed under reflux for 4 hours. The solvent was removed under reduced pressure, and the product was purified by flash column chromatography on silica gel using a 0-25% hexane/ethyl acetate gradient to give **3** as an off-white solid (247 mg, 61%). ^{1}H-NMR (400 MHz $CDCl_3$): δ 7.68-7.62 (m, 6H), 7.52-7.47 (m, 3H), 7.43-7.39 (m, 6H), 6.60 (s, 1H), 2.79-2.76 (t, 4H), 2.51-2.47 (t, 4H), 1.85-1.78 (m, 4H) ppm. ^{13}C-NMR (100 MHz, $CDCl_3$): δ 142.8 (d, J = 2 Hz), 136.4 (d, J = 8 Hz), 134.2, ,133.2, 132.5 (d, J = 10 Hz), 131.2 (d, J = 3 Hz), 128.2 (d, J = 12 Hz), 111.1, 33.5, 32.2, 25.5 ppm. ^{31}P-NMR (162 MHz, $CDCl_3$): 6.09 (s, 1P) ppm. HRMS (ESI) calculated for $C_{30}H_{20}NP$ $[M + H]^+$ 434.2038. Found $[M + H]^+$ 434.2043.

Radiochemistry

Radiochemistry was performed on a Synthra MeI Plus Research module. For the automated synthesis of [^{11}C]MCC950, DMF and DBU were degassed using five freeze-thaw cycles prior to use. Precursor **3** (3.06 mg, 7.07 μmol) was loaded directly into the reactor. 4-(2-hydroxypropan-2-yl)furan-2-sulfonamide **2** (5.86 mg, 28.57 μmol) and KO^{t}Bu (3.14 mg, 27.9 μmol) were weighed in Teflon sealed vials and kept under inert atmosphere. Two minutes prior to the end-of-bombardment, **2** was dissolved in 100

µL of DMF and added to the vial containing KO^{t}Bu. After mixing for 30 seconds, the solution was loaded into the reactor, followed by the addition of DBU (7.46 µL of a 10 µL/mL solution in DMF, 9.97 µmol). The reaction vessel was tightly sealed, and a stream of helium was swept through the reactor after loading. [^{11}C]CO_2 was trapped in a steel coil at -180 ˚C, which was subsequently heated to 25 ˚C under a stream of helium at 3 mL/min to release [^{11}C]CO_2 into the reaction solution until peak activity. The reactor was then heated to 120 ˚C for 3 min prior to addition of 800 µL of mobile phase. For optimization studies, 900 µL of DMF was then added to the reactor and the resulting solution was transferred to a glass vial fitted with a vent needle. The crude reaction was sampled, diluted with water, and analyzed by radioHPLC. Radiochemical conversion (RCC) was determined by integration of radiation detector chromatograms. For preparative studies, the crude reaction mixture was purified by HPLC: Nucleodur C18 Pyramid 7 µm, 250 × 10 mm eluted with 30% ACN/50mM NH_4OAc at 5 mL/min (retention time 6–9 min). The product was collected in a bulk vessel loaded with 25 mL of H_2O and passed through a Sep-Pak C18 Plus Light cartridge. The cartridge was washed with 10 mL of H_2O and eluted with 1.5 mL of EtOH. 13.5 mL of saline was added to the vessel and the contents were passed through a 0.22 µm sterile filter. The identity was established by co-injection with the cold standard using a Waters 2695 Alliance HPLC equipped with a Phenomenex Luna 10 µm C18(2) (100 Å, 250 mm × 4.6 mm) column, a 996-photodiode array detector (Waters), and a Carroll & Ramsey Associates 105-S high-sensitivity radiation detector. Gradient: 80/20 H_2O/ACN for 2 min, linear gradient to 35/65 over 8 min, 35/65 for 2 min, linear gradient to 80/20 for 1 min, 80/20 for 7 min. RCY and A_m values are decay-corrected to end-of-synthesis (EoS). TE was determined from decay-corrected measurements of activity in the steel coil and activity trapped in solution following delivery of [^{11}C]CO_2 into the reactor.

PET imaging

C57BL/6 and *ApoE*$^{-/-}$ mice (12–14 weeks old, 30–45 g) were anesthetized with isoflurane (3%) and placed on the bed of a PET scanner. Following a 10-minute transmission scan, animals were injected with [^{11}C]MCC950 (13 MBq) as a bolus via the lateral vein and maintained under isoflurane during the acquisition. Whole body PET scans were performed for 60 minutes (4 × 15 s frames; 4 × 1 min frames; 10 × 5 min frames) using a Siemens Inveon DPET scanner. The collected emission data were corrected for scatter and attenuation, and reconstructed using the 3-dimensional ordered subsets expectation-maximization/maximum a posteriori (3D-OSEM/MAP) algorithm. Volumes of interest (VOI) were drawn in AMIDE to obtain time-activity curves. Uptake values were obtained in nCi/cc and converted to SUV using total injected dose and animal bodyweight.

Ex vivo biodistribution and autoradiography

C57BL/6 and *ApoE*$^{-/-}$ mice (12–14 weeks old, 30–45 g) were anesthetized with isoflurane (3%) and received lateral tail vein injections of 37–44 MBq of [^{11}C]MCC950 in 0.1–0.2 mL ethanolic saline (10% ethanol in 0.9% sodium chloride). For animals requiring pharmacological challenge, nonradioactive MCC950 (5 mg/kg, 0.9% sodium chloride) was injected via the lateral tail vein 10 minutes prior to radiotracer injection. Fifteen minutes after tracer injection, blood was collected via cardiac puncture and mice were sacrificed by myocardial perfusion. Organs of interest were excised, rinsed in water, weighed, and counted for radioactivity using a Hidex Automatic Gamma counter (energy window: 350–650 keV). Counts per minute (cpm) were converted to activity (nCi) using calibration standards of known activities. Percent injected dose (%ID) was calculated by dividing organ counts (nCi) by the injected dose and further normalized by organ weight to obtain percent injected dose per gram tissue %ID/g. In parallel, aortas harvested from biodistribution were exposed to a super-resolution Storage Phosphor Screen (BAS-IP SR 2025E) in an electrophoresis Systems Autoradiography Cassette (FBXC 810) for 5 h. The screen was

scanned with a Cyclone Plus Storage Phosphor System and images were analyzed using OptiQuant software by drawing aortic arch regions of interest (ROI) that were ORO positive. Digital light units (DLU) were converted to activity (nCi) using calibration standards of known activity. %ID was determined by dividing lesion activity by the injected dose and further normalized by area to obtain activity density in units of %ID/m^2.

Plasma metabolite analysis

Blood samples collected from cardiac puncture at 15 minutes after tracer injection were placed in heparinized tubes and centrifuged at 4 °C for 7 minutes at 4000 rpm to obtain plasma samples. Protein-free plasma (PFP) was obtained by adding an equal volume of ice-cold ACN, followed by centrifugation at 4 °C for 5 min at 4000 rpm. The supernatants were collected, pooled together, and then filtered through a 0.22 µm filter, spiked with nonradioactive standard (10 µL, 1 mg/mL), and injected onto the analytical radioHPLC. Fractions were collected every minute for 20 minutes and the total activity in each fraction was determined by gamma counting.

Plasma free fraction

ApoE$^{-/-}$ mice (12–14 weeks old, 30–45 g) were anesthetized with isoflurane (3%) and received lateral tail vein injections of either cold MCC950 or saline. After 25 minutes, blood was collected via cardiac puncture and the animals were sacrificed. Blood samples were placed in heparinized tubes and centrifuged at 4 °C for 7 minutes at 4000 rpm to obtain plasma samples. Samples were stored at -20 °C prior to use. [^{11}C]MCC950 (3.7 MBq) was added to each sample plus an additional sample containing only PBS and incubated at 37 °C for 10 minutes. The total radioactivity of each sample was measured on a gamma counter. Following incubation, samples were passed through a cellulose centrifugal filter unit with a 30,000 MW cut-off (Centrifree®, Millipore). The filtrate containing plasma free fraction was collected

into a vessel and measured on a gamma counter. The decay-corrected ratio of activity that passed through the filter was calculated and converted into a percentage.

Statistical analysis

Statistical analysis was performed using GraphPad Prism. Data are presented as mean ± standard deviation. Differences between multiple groups were tested using 1-way or 2-way ANOVA with Tukey's multiple comparison test. Significance was set at the 0.05 level.

Results

Radiochemistry

Our recent work highlighted the versatility of iminophosphoranes in synthesizing ^{11}C-labeled compounds, including the sulfonylurea [^{11}C]glyburide in high yield and molar activity, and prompted us to target [^{11}C]MCC950 using this methodology. Indeed, the precursor iminophosphorane (**3**) was easily prepared from commercially available 4-amino-1,2,3,5,6,7-hexahydro-s-indacene (**1**) and triphenylphosphine dibromide in 63% yield using the Kirsanov reaction (see ESI). After combining **3** with furyl sulfonamide **2** and [^{11}C]CO_2 under our previously optimized conditions, we observed an appreciable 42 ± 3% radiochemical conversion (RCC) to [^{11}C]MCC950 with excellent trapping efficiency (TE, Table 1, entry 1). Increasing the reaction temperature to 120 °C improved the RCC to 72 ± 2% and lowering the concentration of iminophosphorane led to a reduced 52 ± 4% RCC (entries 2-3). Higher temperatures facilitated product formation under low precursor loading conditions (entry 4). Reducing the concentration of DBU depressed RCC to 56 ± 2% while retaining the TE. However, the weaker base DABCO diminished the RCC to 9 ± 2% and TE to 52 ± 4% (entry 6), in-line with our previously obtained results using aryl iminophosphoranes. RCC, but not TE, could be restored in the absence of base (entries 7-9). Due to

both milder reaction conditions and quantitative TE, entry 2 was chosen as the optimal conditions for radiotracer production.

Table 1. Optimization of reaction conditions

Entry	Deviation from original conditions[a]	RCC (%)[b]	TE (%)[c]
1	none	42 ± 3	99 ± 2
2	**120 °C**	**72 ± 2**	**99 ± 1**
3	35 mM **3**	52 ± 4	99 ± 3
4	45 mM **3**, 150 °C	63 ± 3	99 ± 0
5	50 mM DBU	56 ± 2	99 ± 2
6	DABCO	9 ± 2	54 ± 1
7	no base, 120 °C	42 ± 3	52 ± 2
8	no base, 150 °C	56 ± 2	58 ± 1
9	no base, 88 mM **3**, 150 °C	82 ± 3	58 ± 2

[a]Original conditions: 70 mM **3**, 285 mM **2**, 100 mM DBU, KO^{t}Bu 280 mM, 100 µL DMF, 100 °C. *n* = 2 per entry. [b]RCC was determined by integration of radioHPLC chromatograms of the crude product. [c]TE was calculated from decay-corrected measurements of initial [^{11}C]CO_2 activity and activity trapped in reactor.

The radiosynthesis of [^{11}C]MCC950 was then performed using a fully automated method on a Synthra MeIplus Research module. From 25.9 GBq of [^{11}C]CO_2, we obtained an isolated RCY of 45 ± 4% (5.18 ± 0.5 GBq) and molar activity (A_m) of 27 ± 2 GBq/µmol within 23 min (Scheme 2), which is suitable for preclinical evaluation. [^{11}C]MCC950 identity was confirmed by coelution with a nonradioactive standard on analytical HPLC, and radiochemical purity was observed to be >99%.

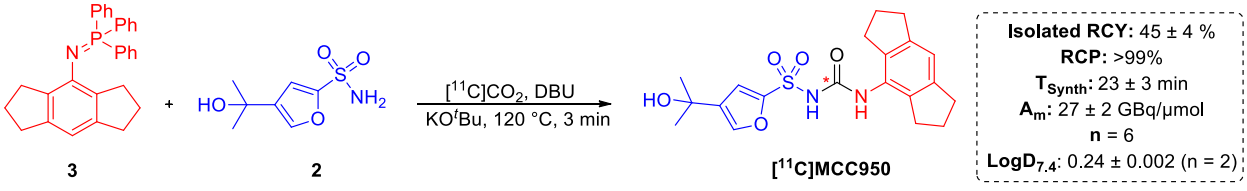

Scheme 2. Automated radiosynthesis of [^{11}C]MCC950.

LogD

Radiotracer lipophilicity was measured by the shake-flask method[26] to uncover the physicochemical properties of the tracer. At physiological pH, [^{11}C]MCC950 bears an anionic charge, and was thus observed to have low lipophilicity ($LogD_{7.4}$ = 0.24 ± 0.002), despite its hydrophobic hexahydro-s-indacene and furan ring systems.

PET imaging and biodistribution

Dynamic PET scans were performed to assess the distribution of [^{11}C]MCC950 in C57BL/6 controls fed normal chow diet, and *ApoE*$^{-/-}$ mice fed Western diet from 6 weeks of age (Figure 1). Blood radioactivity was estimated by VOI placed over the left ventricular cavity. In both strains of mice, blood activity rapidly declined and stabilized at 0.3–0.4 SUV by 10 min**.** In addition, [^{11}C]MCC950 rapidly accumulated in the liver and stabilized by 20 min (7–8.5 SUV). No significant differences in tracer kinetics were observed between C57BL/6 and *ApoE*$^{-/-}$ mice. As previously observed, [^{11}C]MCC950 exhibits no uptake in the brain, and this finding appears to be independent of molar activity.[17] Indeed, other radiotracers containing sulfonylureas have also been shown to have low BBB penetration in animals and humans, likely due to their unfavorable physicochemical properties.[27,28]

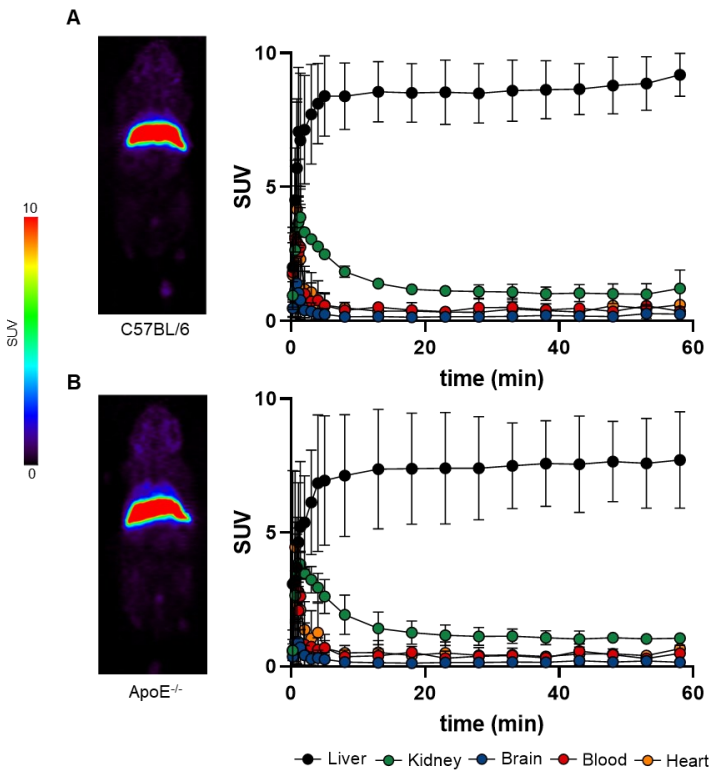

Figure 1: Dynamic PET imaging of [^{11}C]MCC950 in mice. Summed (0–60 min) coronal PET images and time-activity curves for (A) C57BL/6 and (B) *ApoE*$^{-/-}$ mice (*n* = 2 per group).

To determine tracer uptake and the extent of specific binding in lesions, we performed *ex vivo* biodistribution 15 minutes after radiotracer iv tail vein injection, followed by autoradiography of aortas under baseline and blocking conditions. At baseline, C57BL/6 and *ApoE*$^{-/-}$ mice predominantly exhibited hepatic (52.7 ± 16.6 %ID/g vs 24.9 ± 10.3 %ID/g, $p < 0.05$), renal (4.0 ± 0.3 %ID/g vs 8.2 ± 4.3 %ID/g), and intestinal (3.7 ± 0.6 %ID/g vs 5.3 ± 1.8 %ID/g) clearance (Figure 2). Blood radioactivity concentration was similar in C57BL/6 (5.5 ± 3.9 %ID/g) and *ApoE*$^{-/-}$ mice (4.2 ± 1.3 %ID/g). Consistent with our *in vivo* findings, limited uptake of the tracer (<2 %ID/g) was observed in the myocardium, brain, and remaining organs.

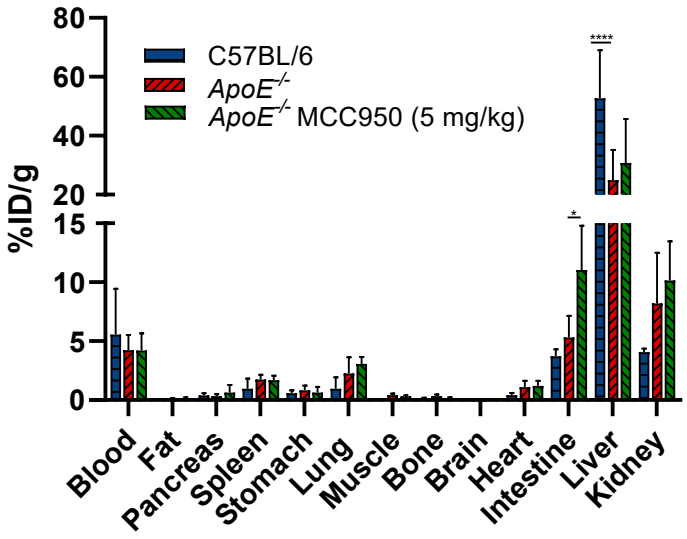

Figure 2. *Ex vivo* biodistribution of [^{11}C]MCC950 15 minutes after radiotracer injection. Two-way ANOVA: *P = 0.04, *n* = 4-5 per group

Homologous blockade was performed in *ApoE*$^{-/-}$ mice using nonradioactive MCC950 (5 mg/kg, iv) 10 minutes prior to administering the radiotracer (Figure 2). Intestinal uptake was increased by two-fold in MCC950 treated mice (11.0 ± 3.7, $p < 0.05$). Otherwise, minimal differences were observed between organs under blocking conditions.

Autoradiography

Following *ex vivo* biodistribution, aortic arch uptake of [^{11}C]MCC950 was visualized by autoradiography and displayed regional uptake in lipid rich Oil red O (ORO) positive atherosclerotic lesions (Figure 3). [^{11}C]MCC950 was found to have 2.7-fold higher uptake in *ApoE*$^{-/-}$ mice compared to C57BL/6 controls (48 ± 17 %ID/m^2 vs 18 ± 8 %ID/m^2, $p = 0.016$). Increased uptake in the lesion aligns with expected findings, as mice kept on Western diet overexpress NLRP3 and its respective inflammasome components.[13,29] In order to determine if tracer uptake within the lesion is specific, homologous blocking was performed as previously described. Animals pretreated with MCC950 displayed a further 2.2-fold

increase in plaque uptake in comparison to untreated animals (104 ± 15 %ID/m^2 vs 48 ± 17 %ID/m^2, p = 0.0002).

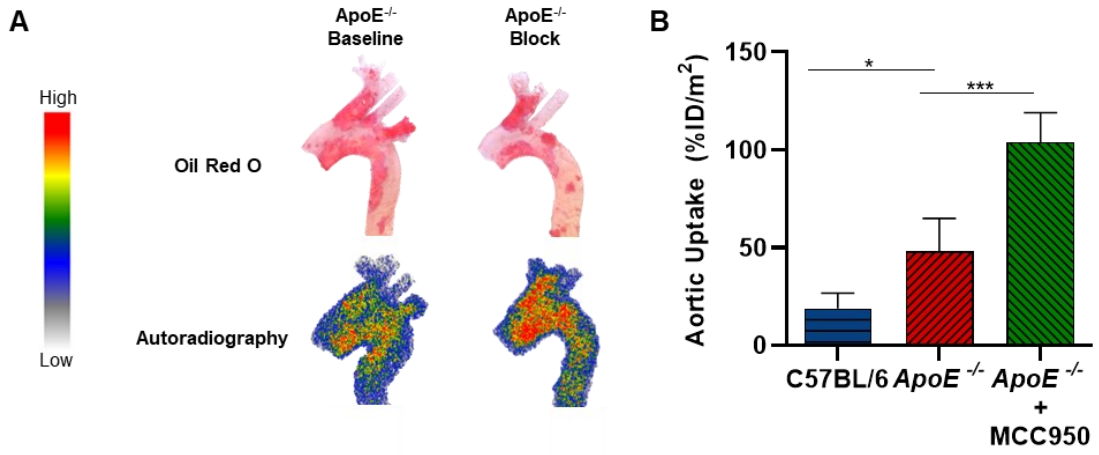

Figure 3. *Ex vivo* aortic autoradiography of [^{11}C]MCC950. (A) Representative ORO brightfield images and autoradiograms after intravenous injection of 37 MBq [^{11}C]MCC950 in *ApoE*$^{-/-}$ mice. Homologous blockade was performed with nonradioactive MCC950 (5 mg/kg, iv) 10 minutes prior to tracer administration. (B) [^{11}C]MCC950 aortic lesion uptake in C57BL/6 and ApoE$^{-/-}$ mice. One-way ANOVA: ***P = 0.0002, *P = 0.002, n = 4-5 per group.

Table 2. [^{11}C]MCC950 plasma stability[a]

Fraction	C57BL/6	*ApoE*$^{-/-}$ baseline	*ApoE*$^{-/-}$ block
Parent radiotracer	92%	94%	93%
Polar metabolites	6%	4%	5%
Non-polar metabolites	2%	2%	2%
Extraction efficiency	92%	91%	92%
Plasma free fraction[b]	n.d.	1.3 ± 0.4%	1.7 ± 0.8%

[a]Percent parent compound of total radioactivity obtained for pooled samples following intravenous tracer administration (n = 5 per group).
[b]Determined *in vitro* (n = 2 per group).

Plasma metabolite analysis

Whole-blood samples collected from *ex vivo* biodistribution at 15 minutes post-injection were pooled for plasma metabolite analysis using fractional radio-HPLC followed by gamma counting. In C57BL/6 and *ApoE*$^{-/-}$mice, 92–94% of the plasma radioactivity corresponded to intact [^{11}C]MCC950, and blocking conditions were observed to have no effect on the metabolic stability of the parent tracer (Table 2). The major metabolite under all conditions was observed to be polar, consistent with previously reported stereospecific ring hydroxylation on the hexahydro-s-indacene moiety.[30] Plasma free fraction (f_p) was then measured for *ApoE*$^{-/-}$ mice under baseline and blocking conditions (Table 2). Under baseline conditions, 1.3 ± 0.4% of the tracer was unbound, and blockade with cold MCC950 (5 mg/kg, iv) led to a moderate but not statistically significant increase of f_p to 1.7 ± 0.8%.

Discussion

MCC950 is a first-in-class NLRP3 inhibitor which has demonstrated considerable promise in resolving inflammation in conditions as diverse as neurodegenerative disorders, myocarditis, and atherosclerosis.[11,12,15,31–35] To evaluate the brain uptake of this inhibitor and to develop a tool for measuring target engagement, Hill *et al.* radiolabeled [^{11}C]MCC950 at low molar activity for PET imaging in several species and found poor brain uptake.[17] Xu *et al.* labeled NLRP3 inhibitors lacking the sulfonylurea moiety, which were observed to have moderate brain uptake (≤1.5 SUV).[36] Despite its lack of CNS penetration, [^{11}C]MCC950 and its derivatives could have profound applications in imaging NLRP3 mediated-inflammation in the periphery.

In atherosclerosis, MCC950 has displayed remarkable use as a therapeutic in significantly reducing plaque area, diminishing the concentration of pro-inflammatory cytokines and macrophages, and improving the lipid profile in *ApoE*$^{-/-}$ mice.[12,37] Previous reports have identified cholesterol crystals in early stages of lesion development to trigger NLRP3-mediated inflammation that is sustained and worsens with

greater plaque progression.[38] Furthermore, NLRP3 expression is observed to be significantly higher in unstable plaques in comparison to stable lesions and has been significantly correlated with atherosclerosis severity scores in humans.[39] As an imaging probe, MCC950 may prove useful in visualizing upregulated NLRP3 expression, discriminating stages of lesion development, and determining plaque stability.

In this work, we prepared [^{11}C]MCC950 with improved molar activity using an operationally simple iminophosphorane precursor for no-carrier-added [^{11}C]CO_2-fixation and evaluated it in a widely used mouse model of atherosclerosis. [^{11}C]MCC950 shows predominant distribution to the liver in both atherosclerotic and control animals, with no accumulation within the brain and fast clearance from other organs. It is highly stable in circulation and is taken up into lipid-rich inflammatory lesions in the aorta. Pretreatment with nonradioactive MCC950 has minimal effect on tissue distribution but augments atherosclerotic lesion uptake by more than two-fold.

Increased uptake in target organs following receptor blockade has been described in the development of CNS radiotracers. This phenomenon may occur due to an increase in radiotracer f_p as a result of plasma protein occupancy by the homologous blocking agent.[40] Consequently, organ activity must be normalized by metabolite-corrected plasma radiotracer levels for accurate estimation of target binding parameters. For example, homologous blockade of the α_2-adrenoceptor antagonist [^{11}C]yohimbine in the rat brain with 0.3 mg/kg of the reference standard decreases binding potentials by 50–60%, but the effect on activity uptake is masked by increased f_p due to saturation of plasma protein binding sites.[41] In addition to plasma normalization, biochemical mechanisms may also explain increased uptake following blockade. Treatment of non-human primates with 4-aminopyridines prior to imaging with the K^+ channel blocker [^{18}F]3F4AP increases volumes of distribution in the brain.[42] An increase in neuronal firing and open, bindable channels is proposed to account for the unanticipated observation. Self-blockade of certain radiolabeled mGluR2 positive allosteric modulators decreases activity uptake across brain regions yet increases volumes of distribution in these same regions. Yuan *et al.* suggest

receptor potentiation towards binding, nonspecific binding, and ligand cooperativity as possible explanations.[43,44] Indeed, similar mechanisms may be at play in the observed increased tracer uptake to aortic plaques following blockade with MCC950.

We surmised that increased plaque uptake of [^{11}C]MCC950 following homologous blockade may be due to drug-induced inflammasome deactivation. The active NLRP3 inflammasome has been reported to undergo a conformational shift promoting disaggregation upon incubation with MCC950, theoretically increasing the number of NLRP3 monomers available for radiotracer binding.[45] Non-specific binding of the tracer is unlikely to contribute to the higher signal observed following blockade based on a moderate 1.3-fold increase in f_p at this dose, compared to 2.2-fold higher tracer uptake in lesions. Accordingly, the more probable hypothesis to explain the observed increased uptake following pretreatment remains an increase in specific binding in plaques. The nature of [^{11}C]MCC950 binding to atherosclerotic plaques *in vivo* could be further evaluated by quantification of NLRP3 monomer concentrations and by challenge dosing with structurally distinct, potent and selective direct NLRP3 inhibitors. Such tools are unfortunately not yet available.

Conclusions

In this study, a high-yielding radiosynthesis for the lead sulfonylurea NLRP3 inhibitor [^{11}C]MCC950 was developed, enabling preclinical evaluation of this compound for imaging atherosclerotic plaques. Radiotracer kinetics were determined by *in vivo* dynamic PET imaging and revealed rapid uptake in the liver and prominent renal excretion. *Ex vivo* biodistribution was also performed at 15 minutes and corroborated these findings. [^{11}C]MCC950 stability studies displayed >90% of the parent tracer intact in plasma, with no differences observed between animal strains. Measurements of f_p demonstrated 1.3 ± 0.4% of the parent unbound to plasma proteins, and a minor increase to 1.7 ± 0.8% unbound following homologous blockade. Last, *ex vivo* autoradiography displayed heterogeneity of lesions within the aortae

of *ApoE*$^{-/-}$ mice, and blockade with cold MCC950 increased plaque uptake by 2.2-fold. Increased retention of the tracer within the lesion following attempted homologous blockade is likely due to a biochemical disaggregation of NLRP3 oligomers, consequently increasing the available monomeric binding sites for [^{11}C]MCC950. This tracer successfully visualized aortic atherosclerotic lesions *ex vivo* and represents the first ^{11}C-labelled sulfonylurea to be evaluated for cardiovascular plaque imaging. Further studies are warranted to explore these findings. The availability of a readily accessible method to synthesize labeled sulfonylureas directly from [^{11}C]CO_2 could enable *in vivo* assessment of novel NLRP3 inhibitors and assist in the development of inflammasome-targeted therapies for inflammatory diseases.

Acknowledgements

The authors thank the staff of the University of Ottawa Heart Institute (UOHI) PET Radiochemistry Laboratory, Biomedical Engineering, and Animal Care and Veterinary Services for cyclotron, small animal PET scanner, and animal care support. The authors acknowledge financial support from CFI (JELF 36848 & 39358), CIHR (PJT 148968), NSERC (RGPIN-2017-06167), and the Ontario Ministry for Research Innovation and Science (ER17-13-119). U.S.I. was supported by Ontario QEII-GSST and the UOHI Endowed Fellowship. A.B. was supported by Ontario OGS, QEII-GSST, and UOHI Endowed Research Scholarship. M.A. was supported by NSERC USRA and University of Ottawa UROP.

Supporting Information

Experimental methods, synthetic procedures, NMR spectra, radiochemistry automation procedures, HPLC chromatograms and calibration curve

Author Contributions

U.S.I. and B.H.R. conceived of the project and prepared the manuscript. U.S.I. performed radiochemistry experiments and analyzed the data. All authors performed biological experiments, contributed to discussion, and edited and approved of the manuscript. B.H.R. directed research.

Declaration of Competing Interest

The authors declare no conflicts of interest.

References

(1) Libby, P.; Buring, J. E.; Badimon, L.; Hansson, G. K.; Deanfield, J.; Bittencourt, M. S.; Tokgözoğlu, L.; Lewis, E. F. Atherosclerosis. *Nat. Rev. Dis. Primer* **2019**, *5* (1), 1–18. https://doi.org/10.1038/s41572-019-0106-z.

(2) Lusis, A. J. Atherosclerosis. *Nature* **2000**, *407* (6801), 233–241. https://doi.org/10.1038/35025203.

(3) Shah, P.; Bajaj, S.; Virk, H.; Bikkina, M.; Shamoon, F. Rapid Progression of Coronary Atherosclerosis: A Review. *Thrombosis* **2015**, *2015*, e634983. https://doi.org/10.1155/2015/634983.

(4) Karasawa, T.; Takahashi, M. Role of NLRP3 Inflammasomes in Atherosclerosis. *J. Atheroscler. Thromb.* **2017**, *24* (5), 443–451. https://doi.org/10.5551/jat.RV17001.

(5) Stitham, J.; Rodriguez-Velez, A.; Zhang, X.; Jeong, S.-J.; Razani, B. Inflammasomes: A Preclinical Assessment of Targeting in Atherosclerosis. *Expert Opin. Ther. Targets* **2020**, *24* (9), 825–844. https://doi.org/10.1080/14728222.2020.1795831.

(6) Jin, Y.; Fu, J. Novel Insights Into the NLRP3 Inflammasome in Atherosclerosis. *J. Am. Heart Assoc.* **2019**, *8* (12), e012219. https://doi.org/10.1161/JAHA.119.012219.

(7) Grebe, A.; Hoss, F.; Latz, E. NLRP3 Inflammasome and the IL-1 Pathway in Atherosclerosis. *Circ. Res.* **2018**, *122* (12), 1722–1740. https://doi.org/10.1161/CIRCRESAHA.118.311362.

(8) Duewell, P.; Kono, H.; Rayner, K. J.; Sirois, C. M.; Vladimer, G.; Bauernfeind, F. G.; Abela, G. S.; Franchi, L.; Nuñez, G.; Schnurr, M.; Espevik, T.; Lien, E.; Fitzgerald, K. A.; Rock, K. L.; Moore, K. J.; Wright, S. D.; Hornung, V.; Latz, E. NLRP3 Inflammasomes Are Required for Atherogenesis and Activated by Cholesterol Crystals. *Nature* **2010**, *464* (7293), 1357–1361. https://doi.org/10.1038/nature08938.

(9) Usui, F.; Shirasuna, K.; Kimura, H.; Tatsumi, K.; Kawashima, A.; Karasawa, T.; Hida, S.; Sagara, J.; Taniguchi, S.; Takahashi, M. Critical Role of Caspase-1 in Vascular Inflammation and Development of Atherosclerosis in Western Diet-Fed Apolipoprotein E-Deficient Mice. *Biochem. Biophys. Res. Commun.* **2012**, *425* (2), 162–168. https://doi.org/10.1016/j.bbrc.2012.07.058.

(10) Gage, J.; Hasu, M.; Thabet, M.; Whitman, S. C. Caspase-1 Deficiency Decreases Atherosclerosis in Apolipoprotein E-Null Mice. *Can. J. Cardiol.* **2012**, *28* (2), 222–229. https://doi.org/10.1016/j.cjca.2011.10.013.

(11) van der Heijden, T.; Kritikou, E.; Venema, W.; van Duijn, J.; van Santbrink, P. J.; Slütter, B.; Foks, A. C.; Bot, I.; Kuiper, J. NLRP3 Inflammasome Inhibition by MCC950 Reduces Atherosclerotic Lesion

Development in Apolipoprotein E–Deficient Mice—Brief Report. *Arterioscler. Thromb. Vasc. Biol.* **2017**, *37* (8), 1457–1461. https://doi.org/10.1161/ATVBAHA.117.309575.
(12) Sharma, A.; Choi, J. S. Y.; Stefanovic, N.; Al-Sharea, A.; Simpson, D. S.; Mukhamedova, N.; Jandeleit-Dahm, K.; Murphy, A. J.; Sviridov, D.; Vince, J. E.; Ritchie, R. H.; de Haan, J. B. Specific NLRP3 Inhibition Protects Against Diabetes-Associated Atherosclerosis. *Diabetes* **2020**, *70* (3), 772–787. https://doi.org/10.2337/db20-0357.
(13) Zeng, W.; Wu, D.; Sun, Y.; Suo, Y.; Yu, Q.; Zeng, M.; Gao, Q.; Yu, B.; Jiang, X.; Wang, Y. The Selective NLRP3 Inhibitor MCC950 Hinders Atherosclerosis Development by Attenuating Inflammation and Pyroptosis in Macrophages. *Sci. Rep.* **2021**, *11* (1), 19305. https://doi.org/10.1038/s41598-021-98437-3.
(14) Hettwer, J.; Hinterdobler, J.; Miritsch, B.; Deutsch, M.-A.; Li, X.; Mauersberger, C.; Moggio, A.; Braster, Q.; Gram, H.; Robertson, A. A. B.; Cooper, M. A.; Groß, O.; Krane, M.; Weber, C.; Koenig, W.; Soehnlein, O.; Adamstein, N. H.; Ridker, P.; Schunkert, H.; Libby, P.; Kessler, T.; Sager, H. B. Interleukin-1β Suppression Dampens Inflammatory Leucocyte Production and Uptake in Atherosclerosis. *Cardiovasc. Res.* **2021**, cvab337. https://doi.org/10.1093/cvr/cvab337.
(15) Coll, R. C.; Robertson, A. A. B.; Chae, J. J.; Higgins, S. C.; Muñoz-Planillo, R.; Inserra, M. C.; Vetter, I.; Dungan, L. S.; Monks, B. G.; Stutz, A.; Croker, D. E.; Butler, M. S.; Haneklaus, M.; Sutton, C. E.; Núñez, G.; Latz, E.; Kastner, D. L.; Mills, K. H. G.; Masters, S. L.; Schroder, K.; Cooper, M. A.; O'Neill, L. A. J. A Small-Molecule Inhibitor of the NLRP3 Inflammasome for the Treatment of Inflammatory Diseases. *Nat. Med.* **2015**, *21* (3), 248–255. https://doi.org/10.1038/nm.3806.
(16) Li, H.; Guan, Y.; Liang, B.; Ding, P.; Hou, X.; Wei, W.; Ma, Y. Therapeutic Potential of MCC950, a Specific Inhibitor of NLRP3 Inflammasome. *Eur. J. Pharmacol.* **2022**, *928*, 175091. https://doi.org/10.1016/j.ejphar.2022.175091.
(17) Hill, J. R.; Shao, X.; Massey, N. L.; Stauff, J.; Sherman, P. S.; Robertson, A. A. B.; Scott, P. J. H. Synthesis and Evaluation of NLRP3-Inhibitory Sulfonylurea [11C]MCC950 in Healthy Animals. *Bioorg. Med. Chem. Lett.* **2020**, *30* (12), 127186. https://doi.org/10.1016/j.bmcl.2020.127186.
(18) Nerella, S. G.; Singh, P.; Tulja, S. Carbon-11 Patents (2012–2022): Synthetic Methodologies and Novel Radiotracers for PET Imaging. *Expert Opin. Ther. Pat.* **2022**, *32* (7), 817–831. https://doi.org/10.1080/13543776.2022.2070003.
(19) Rotstein, B. H.; Liang, S. H.; Placzek, M. S.; Hooker, J. M.; Gee, A. D.; Dollé, F.; Wilson, A. A.; Vasdev, N. 11CO Bonds Made Easily for Positron Emission Tomography Radiopharmaceuticals. *Chem. Soc. Rev.* **2016**, *45* (17), 4708–4726. https://doi.org/10.1039/C6CS00310A.
(20) Taddei, C.; Pike, V. W. [11C]Carbon Monoxide: Advances in Production and Application to PET Radiotracer Development over the Past 15 Years. *EJNMMI Radiopharm. Chem.* **2019**, *4* (1), 25. https://doi.org/10.1186/s41181-019-0073-4.
(21) Villa, A.; Klein, B.; Janssen, B.; Pedragosa, J.; Pepe, G.; Zinnhardt, B.; Vugts, D. J.; Gelosa, P.; Sironi, L.; Beaino, W.; Damont, A.; Dollé, F.; Jego, B.; Winkeler, A.; Ory, D.; Solin, O.; Vercouillie, J.; Funke, U.; Laner-Plamberger, S.; Blomster, L. V.; Christophersen, P.; Vegeto, E.; Aigner, L.; Jacobs, A.; Planas, A. M.; Maggi, A.; Windhorst, A. D. Identification of New Molecular Targets for PET Imaging of the Microglial Anti-Inflammatory Activation State. *Theranostics* **2018**, *8* (19), 5400–5418. https://doi.org/10.7150/thno.25572.
(22) Åberg, O.; Långström, B. Synthesis of Substituted [11C]Ureas and [11C]Sulphonylureas by Rh(I)-Mediated Carbonylation. *J. Label. Compd. Radiopharm.* **2011**, *54* (1), 38–42. https://doi.org/10.1002/jlcr.1803.
(23) Wilson, A. A.; Garcia, A.; Houle, S.; Sadovski, O.; Vasdev, N. Synthesis and Application of Isocyanates Radiolabeled with Carbon-11. *Chem. – Eur. J.* **2011**, *17* (1), 259–264. https://doi.org/10.1002/chem.201002345.

(24) Dheere, A. K. H.; Yusuf, N.; Gee, A. Rapid and Efficient Synthesis of [11C]Ureas via the Incorporation of [11C]CO2 into Aliphatic and Aromatic Amines. *Chem. Commun.* **2013**, *49* (74), 8193–8195. https://doi.org/10.1039/C3CC44046J.
(25) Ismailani, U. S.; Munch, M.; Mair, B. A.; Rotstein, B. H. Interrupted Aza-Wittig Reactions Using Iminophosphoranes to Synthesize ^{11}C–Carbonyls. *Chem. Commun.* **2021**, 10.1039.D1CC01016F. https://doi.org/10.1039/D1CC01016F.
(26) Wilson, A. A.; Jin, L.; Garcia, A.; DaSilva, J. N.; Houle, S. An Admonition When Measuring the Lipophilicity of Radiotracers Using Counting Techniques. *Appl. Radiat. Isot.* **2001**, *54* (2), 203–208. https://doi.org/10.1016/S0969-8043(00)00269-4.
(27) van der Wildt, B.; Janssen, B.; Pekošak, A.; Stéen, E. J. L.; Schuit, R. C.; Kooijman, E. J. M.; Beaino, W.; Vugts, D. J.; Windhorst, A. D. Novel Thienopyrimidine-Based PET Tracers for P2Y12 Receptor Imaging in the Brain. *ACS Chem. Neurosci.* **2021**, *12* (23), 4465–4474. https://doi.org/10.1021/acschemneuro.1c00641.
(28) Marie, S.; Comtat, C.; Caillé, F.; Becquemont, L.; Bottlaender, M.; Tournier, N. 11C-Glyburide PET Imaging Unveils the Negligible Brain Penetration of Glyburide in Humans. *Neurology* **2019**, *92* (17), 813–814. https://doi.org/10.1212/WNL.0000000000007378.
(29) Wang, R.; Wang, Y.; Mu, N.; Lou, X.; Li, W.; Chen, Y.; Fan, D.; Tan, H. Activation of NLRP3 Inflammasomes Contributes to Hyperhomocysteinemia-Aggravated Inflammation and Atherosclerosis in ApoE-Deficient Mice. *Lab. Invest.* **2017**, *97* (8), 922–934. https://doi.org/10.1038/labinvest.2017.30.
(30) Salla, M.; Butler, M. S.; Pelingon, R.; Kaeslin, G.; Croker, D. E.; Reid, J. C.; Baek, J. M.; Bernhardt, P. V.; Gillam, E. M. J.; Cooper, M. A.; Robertson, A. A. B. Identification, Synthesis, and Biological Evaluation of the Major Human Metabolite of NLRP3 Inflammasome Inhibitor MCC950. *ACS Med. Chem. Lett.* **2016**, *7* (12), 1034–1038. https://doi.org/10.1021/acsmedchemlett.6b00198.
(31) Hull, C.; Dekeryte, R.; Buchanan, H.; Kamli-Salino, S.; Robertson, A.; Delibegovic, M.; Platt, B. NLRP3 Inflammasome Inhibition with MCC950 Improves Insulin Sensitivity and Inflammation in a Mouse Model of Frontotemporal Dementia. *Neuropharmacology* **2020**, *180*, 108305. https://doi.org/10.1016/j.neuropharm.2020.108305.
(32) Gordon, R.; Albornoz, E. A.; Christie, D. C.; Langley, M. R.; Kumar, V.; Mantovani, S.; Robertson, A. A. B.; Butler, M. S.; Rowe, D. B.; O'Neill, L. A.; Kanthasamy, A. G.; Schroder, K.; Cooper, M. A.; Woodruff, T. M. Inflammasome Inhibition Prevents α-Synuclein Pathology and Dopaminergic Neurodegeneration in Mice. *Sci. Transl. Med.* **2018**, *10* (465), eaah4066. https://doi.org/10.1126/scitranslmed.aah4066.
(33) Chen, K.-P.; Hua, K.-F.; Tsai, F.-T.; Lin, T.-Y.; Cheng, C.-Y.; Yang, D.-I.; Hsu, H.-T.; Ju, T.-C. A Selective Inhibitor of the NLRP3 Inflammasome as a Potential Therapeutic Approach for Neuroprotection in a Transgenic Mouse Model of Huntington's Disease. *J. Neuroinflammation* **2022**, *19* (1), 56. https://doi.org/10.1186/s12974-022-02419-9.
(34) Ren, P.; Wu, D.; Appel, R.; Zhang, L.; Zhang, C.; Luo, W.; Robertson, A. A. B.; Cooper, M. A.; Coselli, J. S.; Milewicz, D. M.; Shen, Y. H.; LeMaire, S. A. Targeting the NLRP3 Inflammasome With Inhibitor MCC950 Prevents Aortic Aneurysms and Dissections in Mice. *J. Am. Heart Assoc.* **2020**, *9* (7), e014044. https://doi.org/10.1161/JAHA.119.014044.
(35) Li, X.; Yang, W.; Ma, W.; Zhou, X.; Quan, Z.; Li, G.; Liu, D.; Zhang, Q.; Han, D.; Gao, B.; Li, C.; Wang, J.; Kang, F. 18F-FDG PET Imaging-Monitored Anti-Inflammatory Therapy for Acute Myocardial Infarction: Exploring the Role of MCC950 in Murine Model. *J. Nucl. Cardiol.* **2021**, *28* (5), 2346–2357. https://doi.org/10.1007/s12350-020-02044-0.
(36) Xu, Y.; Xu, Y.; Blevins, H.; Lan, Y.; Liu, Y.; Yuan, G.; Striar, R.; Zagaroli, J. S.; Tocci, D. R.; Langan, A. G.; Zhang, C.; Zhang, S.; Wang, C. Discovery of Carbon-11 Labeled Sulfonamide Derivative: A PET Tracer

for Imaging Brain NLRP3 Inflammasome. *Bioorg. Med. Chem. Lett.* **2021**, *34*, 127777. https://doi.org/10.1016/j.bmcl.2021.127777.
(37) Ma, Q.; Fan, Q.; Han, X.; Dong, Z.; Xu, J.; Bai, J.; Tao, W.; Sun, D.; Wang, C. Platelet-Derived Extracellular Vesicles to Target Plaque Inflammation for Effective Anti-Atherosclerotic Therapy. *J. Controlled Release* **2021**, *329*, 445–453. https://doi.org/10.1016/j.jconrel.2020.11.064.
(38) Baldrighi, M.; Mallat, Z.; Li, X. NLRP3 Inflammasome Pathways in Atherosclerosis. *Atherosclerosis* **2017**, *267*, 127–138. https://doi.org/10.1016/j.atherosclerosis.2017.10.027.
(39) Liu, Y.; Li, C.; Yin, H.; Zhang, X.; Li, Y. NLRP3 Inflammasome: A Potential Alternative Therapy Target for Atherosclerosis. *Evid.-Based Complement. Altern. Med. ECAM* **2020**, *2020*, 1561342. https://doi.org/10.1155/2020/1561342.
(40) Van de Bittner, G. C.; Ricq, E. L.; Hooker, J. M. A Philosophy for CNS Radiotracer Design. *Acc. Chem. Res.* **2014**, *47* (10), 3127–3134. https://doi.org/10.1021/ar500233s.
(41) Phan, J.-A.; Landau, A. M.; Jakobsen, S.; Wong, D. F.; Gjedde, A. Radioligand Binding Analysis of A2 Adrenoceptors with [11C]Yohimbine in Brain in Vivo: Extended Inhibition Plot Correction for Plasma Protein Binding. *Sci. Rep.* **2017**, *7* (1), 15979. https://doi.org/10.1038/s41598-017-16020-1.
(42) Guehl, N. J.; Ramos-Torres, K. M.; Linnman, C.; Moon, S.-H.; Dhaynaut, M.; Wilks, M. Q.; Han, P. K.; Ma, C.; Neelamegam, R.; Zhou, Y.-P.; Popko, B.; Correia, J. A.; Reich, D. S.; Fakhri, G. E.; Herscovitch, P.; Normandin, M. D.; Brugarolas, P. Evaluation of the Potassium Channel Tracer [18F]3F4AP in Rhesus Macaques. *J. Cereb. Blood Flow Metab.* **2021**, *41* (7), 1721–1733. https://doi.org/10.1177/0271678X20963404.
(43) Yuan, G.; Guehl, N. J.; Zheng, B.; Qu, X.; Moon, S.-H.; Dhaynaut, M.; Shoup, T. M.; Afshar, S.; Kang, H. J.; Zhang, Z.; El Fakhri, G.; Normandin, M. D.; Brownell, A.-L. Synthesis and Characterization of [18F]JNJ-46356479 as the First 18F-Labeled PET Imaging Ligand for Metabotropic Glutamate Receptor 2. *Mol. Imaging Biol.* **2021**, *23* (4), 527–536. https://doi.org/10.1007/s11307-021-01586-0.
(44) Yuan, G.; Dhaynaut, M.; Guehl, N. J.; Afshar, S.; Huynh, D.; Moon, S.-H.; Iyengar, S. M.; Jain, M. K.; Pickett, J. E.; Kang, H. J.; Ondrechen, M. J.; El Fakhri, G.; Normandin, M. D.; Brownell, A.-L. Design, Synthesis, and Characterization of [18F]MG2P026 as a High-Contrast PET Imaging Ligand for Metabotropic Glutamate Receptor 2. *J. Med. Chem.* **2022**, *65* (14), 9939–9954. https://doi.org/10.1021/acs.jmedchem.2c00593.
(45) Tapia-Abellán, A.; Angosto-Bazarra, D.; Martínez-Banaclocha, H.; de Torre-Minguela, C.; Cerón-Carrasco, J. P.; Pérez-Sánchez, H.; Arostegui, J. I.; Pelegrin, P. MCC950 Closes the Active Conformation of NLRP3 to an Inactive State. *Nat. Chem. Biol.* **2019**, *15* (6), 560–564. https://doi.org/10.1038/s41589-019-0278-6.